Nondestructive On-Site Detection of Soybean Contents Based on An Electrothermal MEMS Fourier Transform Spectrometer
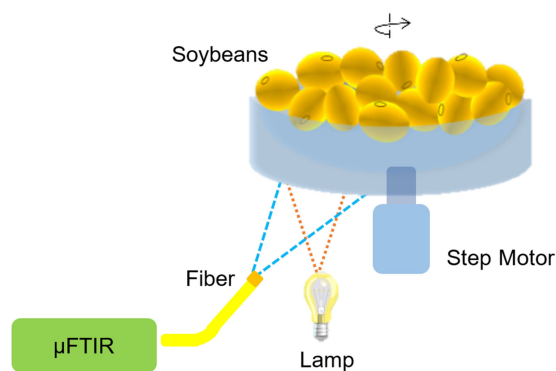
Donglin Wang
Peng Wang
Huan Liu
Hongqiong Liu
Jicheng Zhang
Weiguo Liu
Huikai Xie, *Fellow, IEEE*

Nondestructive On-Site Detection of Soybean Contents Based on An Electrothermal MEMS Fourier Transform Spectrometer

Donglin Wang [iD],[1] **Peng Wang,**[1] **Huan Liu,**[1] **Hongqiong Liu,**[2] **Jicheng Zhang,**[2] **Weiguo Liu,**[1] **and Huikai Xie** [iD],[1,3] *Fellow, IEEE*

[1]School of Optoelectronic Engineering, Xi'an Technological University, Xi'an 710021, China
[2]Wuxi WiO Technologies Co., Ltd., Wuxi 214000, China
[3]University of Florida, Gainesville, FL 32611 USA

Abstract: A portable spectrophotometer has been developed to provide on-site detection of soybeans' moisture, protein, and fat contents in a nondestructive manner. The core module of this soybean analyzer is a micro Fourier transform infrared spectrometer (μFTIR) based on an electrothermal microelectromechanical systems (MEMSs) mirror. The electrothermal MEMS mirror is capable of generating a large piston motion of 320 μm at only 8.5 Vdc. The tilting of the MEMS mirror plate during its piston scanning affects the spectral repeatability of the μFTIR. In this paper, the effect of the MEMS mirror tilting on the spectral repeatability is analyzed and an automatic tilt realignment algorithm is developed to maintain high spectral repeatability, which is better than 0.01 in long term use. The μFTIR module has a footprint of 125 mm $\times$ 90 mm with a height of 50 mm. The whole instrument is designed for portability and on-site operation as well as the convenience of loading soybeans. More than 300 samples of soybeans are collected, 80% of which are used to establish a prediction model using chemometrics methods. The standard error is no more than 3% when using the prediction model to test the remaining 20% samples.

Index Terms: MEMS mirror, FTIR, NIR spectroscopy, chemometrics, electrothermal actuation, soybean analyzer.

1. Introduction

Soybeans are a significant source of plant oils and proteins and widely used in food and industrial productions. Accurate determination of the contents of soybeans is very important, especially in international trades where the price of soybeans is determined by the protein content. The moisture, protein and fat concentrations in soybeans can be obtained by using oven drying, Kjeldahl nitrogen method, and Soxhlet extraction, respectively [1]. These methods are accurate but not convenient for on-line or on-site measurement since bulky equipment is needed and the procedures typically take long time.

Near-infrared spectroscopy (NIRS) uses absorption spectra from 780 nm to 2500 nm to provide quantitative determination or qualitative discrimination for sample analysis. It is based on the vibrations of molecular bonds such as C-H, N-H, or O-H and the absorption spectrum in near infrared has strong correlation with the contents of the sample. Although the molecular overtone and combination bands in NIRS are typically broad and it is difficult to identify specific chemical components, regression algorithms have been developed to extract the desired information successfully [2]. The advantages of fast, nondestructive and multi-parameter measurement make NIRS gain a wide range of applications. For instance, NIRS has been successfully applied in agricultural and food analysis for decades [3], [4]. As the demand of rapid on-site detection is increasing, NIRS is no longer limited in laboratory use; it starts to step into farmland scenes. Thus, miniaturization, portability and low cost are the current trend for NIRS development.

Microelectromechanical systems (MEMS) is a powerful technology that has the advantages of small size, fast speed and low cost. It is capable of miniaturizing spectrometers and various MEMS based spectrometers have been developed [5], [6]. MEMS spectrometers can be classified into three categories: dispersive gratings [7]–[9], tunable filters [10]–[12], and Fourier transform infrared (FTIR) spectrometers [13]–[16]. MEMS-based FTIR, or μFTIR, has the advantages of higher signal to noise ratio (SNR) and spectral resolution as well as potentially low cost as only single IR photodetectors, instead of expensive IR detector arrays, are needed. Several groups have investigated MEMS scanning mirrors with various actuation mechanisms to implement μFTIR [17]–[20]. Compared with electrostatic and electromagnetic actuators, electrothermal bimorph actuators have a clear advantage of large linear scan range without the need of complex resonance operation [21]. By using a properly tuned driving setting and a phase interpolation algorithm, large piston and small tilting angle without closed-loop control are simultaneously achieved with such electrothermal MEMS mirrors [22]. Several μFTIR systems based on the electrothermal MEMS mirrors have been demonstrated [23], [24].

In this work, a compact μFTIR module based on an electrothermal mirror with a #-shaped mirror plate, abbreviated as ET-μFTIR, has been developed and employed to make a soybean analyzer. In this paper, the ET-μFTIR module is described in Section 2, including the ET-μFTIR architecture design, the MEMS mirror, and the characterization result of the ET-μFTIR module. The analysis of the issues in on-site detection applications and the corresponding strategy are also explained in Section 2. Then the product design and performance evaluation of the soybean analyzer are presented in Section 3.

2. Design and Analysis of the ET-μFTIR

2.1 Architecture of the ET- μFTIR

The core of the ET-μFTIR consists of two Michelson interferometers (MI) as sketched in Fig. 1(a), where an electrothermal MEMS mirror (MM) is located in between two beam splitters (BS). Both the front- and back- surfaces of the mirror plate of the MEMS mirror are highly reflective and together with two fixed mirrors (FM) a dual Michelson interferometer (DMI) configuration is formed. One MI generates interferograms from samples while the other MI provides interference fringes for tracking the position of the mirror plate in real time. Fig. 1(b) is a picture of an actually-constructed DMI, where a group of double lenses (DL) focuses the sample light from an SMA fiber connector into the right-hand side of the MEMS mirror (MM), and a BS separates a portion of the sample light into an FM. An InGaAs photodetector (PD1), with a spectral response range of 900 nm to 2500 nm, picks up the sample interferogram signals. A 1310 nm laser, collimated by a fiber pigtail gradient index lens, is directed to the other side of the MEMS mirror as a reference light. This laser is chosen because of its small size and pigtail type. Other pigtailed lasers may be used as well depending on availability. Another photodetector (PD2) with the spectral response range from 900 nm to 1700 nm is used to receive the reference interferogram. As shown in Fig. 1(a), the fixed mirrors in the DMI are all placed on the same side to simplify the assembling process. Although the DMI configuration is similar to the one previously reported in [22], this DMI has a more compact structure and the size
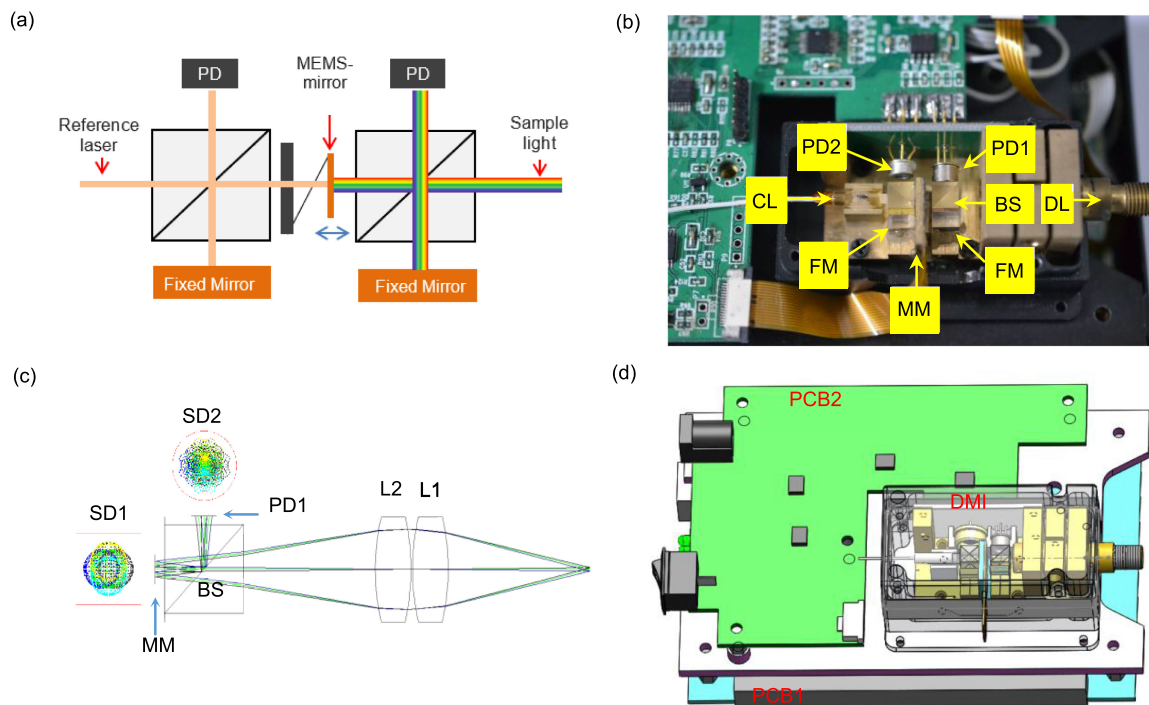
Fig. 1. (a) Schematic of the DMI optical core. (b) Photo of the optical core. (c) Optical design of the MI for samples. (d) 3D design of the ET-μFTIR. PD: photodetector. MM: MEMS mirror. BS: beamsplitter. SD: spot diameter. CL: collimating lens. DL: double lenses. FM: fixed mirror. PCB: printed circuit board. DMI: dual Michelson interferometer.

of the optical core is only 50 mm $\times$ 30 mm $\times$ 27 mm, which is reduced by a factor of 4 from that in [22]. The optical design of the double lenses is optimized using Code V [25] and is presented in Fig. 1(c), where L1 and L2 are the same bi-convex spherical singlet (LB1406 Thorlabs). The spot diameter SD1 on the MEMS mirror is 0.8 mm, which is smaller than the rectangular mirror plate as the red square depicts. The diameter of the photosensitive area of PD1 is also larger than the spot diameter SD2. The 3D model of the entire design of the ET-μFTIR is shown in Fig. 1(d), where two printed circuit boards (PCB1 and PCB2) are used. PCB1 outputs four driving signals for the MEMS mirror and acquire two interferograms from the DMI. PCB2 provides all power supplies as well as the filters for the driving waveforms.

2.2 Electrothermal MEMS Mirror

Double layers of materials, or bimorph layers, with different coefficients of thermal expansion (CTEs) are commonly used for making electrothermal microactuators. As Fig. 2(a) depicts, when temperature changes, a bimorph beam will bend due to the CTE difference. To implement variable temperature, a resistor is often embedded in the bimorph beam. When an electrical current passes through the resistor, Joule heating will be generated, which in turn will change the temperature of the bimorph. This is called electrothermal bimorph actuation. In this work, aluminum (Al) and silicon dioxide (SiO$_2$) are chosen as the bimorph materials due to their large CTE difference which can lead to large displacement. The CTEs of Al, SiO$_2$ and Si are 23.3 10^{-6}/K, 0.5 10^{-6}/K, and 2.6 10^{-6}/K, respectively. As Al has much higher CTE than both SiO$_2$ and Si, the Al layer deposited on top of SiO$_2$ and Si at an elevated temperature will tend to shrink when cooled down to room temperature. Thus, once the silicon layer is removed, i.e., the bimorph is released, the bimorph tends to bend toward the Al side. When the temperature increases, the bimorph will bend back
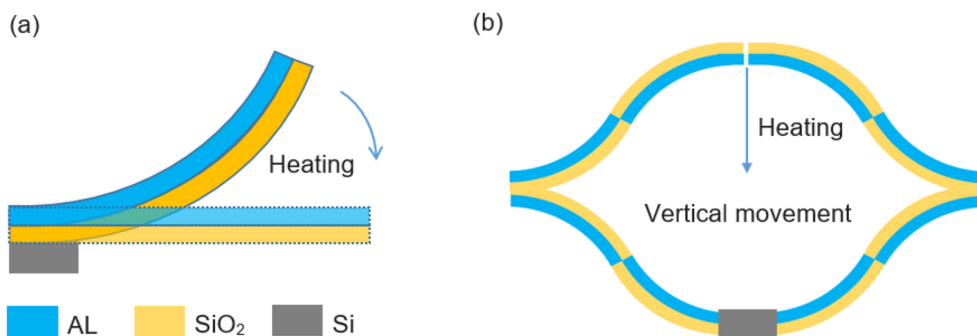
Fig. 2. (a) Thermal bimorph actuation. (b) Schematic of the bilaterally symmetrical FDSB electrothermal bimorph actuator.
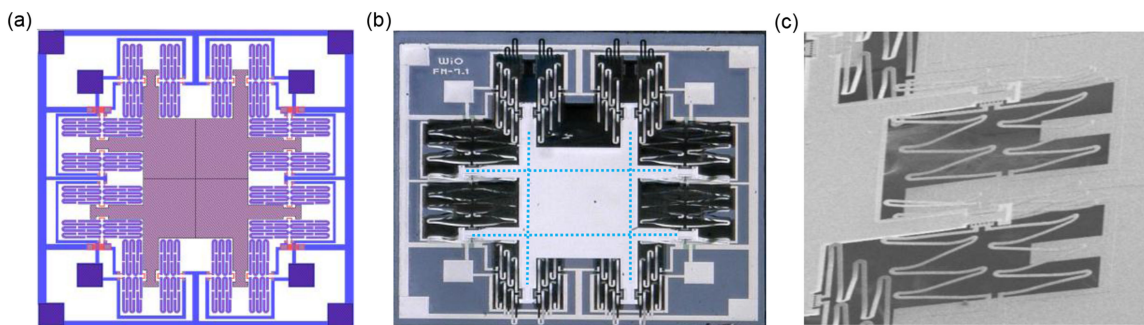

Fig. 3. (a) Topology design of the MEMS mirror. (b) Photo of the MEMS mirror, and dash lines depict the shape of mirror plate is a #-type. (c) SEM of the FDSB actuators.

toward the SiO_2 side, as shown in Fig. 2(a), Fig. 2(b) shows one ladder of an electrothermal Al/SiO_2 bimorph actuator design. It has bilaterally-symmetrical four sections of alternating bimorphs and each side forms a folded double S-shaped bimorph (FDSB) structure [26]. Al has higher CTE, so the initial curling of each bimorph section bends toward the Al side. By increasing the temperature, the bimorph will bend to the SiO_2 side as it has lower CTE. The symmetrical design can compensate lateral shift, so the FDSB actuator can produce pure vertical displacement.

Fig. 3(a) is the topology design of the MEMS mirror with large piston motion for the μFTIR. It consists of a central mirror plate and 16 three-level FDSB actuators around it. The three-level FDSB actuator design is employed to increase the displacement range [27]. Two rigid cantilever beams extended from each corner of the mirror plate are designed to connect 2 three-level FDSB actuators each. To fabricate the MEMS mirror a hybrid bulk and surface micromachining process on SOI wafer is used. The fabrication mainly includes SiO_2 and Al deposition and patterning for bimorph structures, titanium (Ti) deposition and patterning for embedded heaters, and silicon DRIE for device releasing [24]. Fig. 3(b) presents a photo of the MEMS mirror (FM-7.1, WiO Tech), where the mirror plate is 1.5 mm $\times$ 1.2 mm in size and suspended 300 μm over the substrate surface by 16 three-level FDSB actuators. An SEM picture in Fig. 3(c) shows the detail of a pair of three-level FDSB actuators.

Encapsulating the MEMS mirror is also important for minimizing ambient environment disturbances. Simply sealing the MEMS mirror in a chamber with a sapphire window and filling the chamber with nitrogen can improve the scanning stability of the MEMS mirror. Fig. 4(a) shows a packaged MEMS mirror that is wire bonded to a flexible PCB attached in a copper case. Fig. 4(b) shows the displacements at various dc voltages, where a maximum displacement of 320 μm is obtained at 8.5 Vdc. The displacement is induced by a series of effects once an electrical current
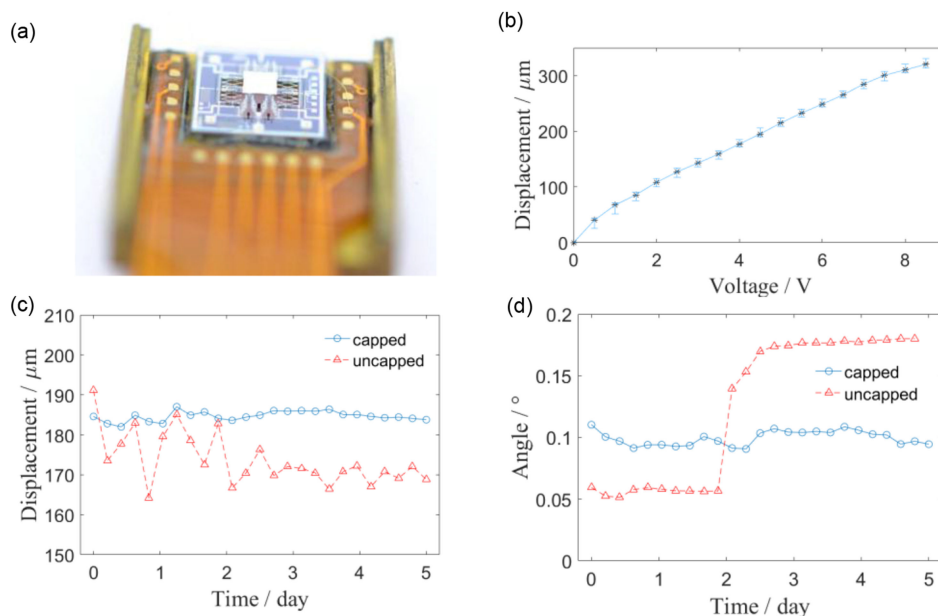
(a)

(b)

(c)

(d)

Fig. 4. (a) Photo of a packaged MEMS mirror. (b) Displacement versus voltage of the MEMS mirror. (c) MEMS motion displacement (at 6.5 V) over time. (d) Tilting angle of MEMS mirror versus time.

is injected into a resistor, leading to i.e., Joule heating, temperature rise, thermal stress, bimorph bending, and finally a displacement at the end of the bimorph actuator. The theoretical modeling of this response is out of the scope of this paper, but interested readers may refer to [29]. Fig. 4(c) plots the displacements over time for a capped MEMS and an uncapped MEMS, respectively, showing that the displacement variation of the capped type is reduced down to 5 μm from the uncapped MEMS's 30 μm. Similarly, the tilting angle of the capped MEMS is more stable and the maximum variation is only 0.02°.

2.3 Characteristics of the ET-μFTIR

2.3.1 Spectral Repeatability: Spectral repeatability is one of the most critical characteristics of spectrometers for quantitative analysis. Typically a number of spectra are acquired to calculate the spectral repeatability, which is given by

$$\frac{1}{N} \sum_{j=1}^{N} \sqrt{\frac{\sum_{i=1}^{n} \left(A_i^j - \overline{A^j}\right)^2}{n-1}} \tag{1}$$

where n is the number of spectra acquired, N is the number of wavelengths of each spectrum, determined by the number of interpolation points when the spectrum is recovered by Fourier transform from an interferogram, A_i^j stands for the absorption of the ith spectrum at the jth wavelength (i = 1, 2, ... n; j = 1, 2, ..., N), and $\overline{A^j}$ stands for the averaged absorption at the jth wavelength. Typically, n is set at 10, which means the calculation is based on 10 resampled absorption spectra, and N is 15,000 for the spectral range of 1000 nm to 2500 nm used for the soybean application, which means the wavelength interval is 0.1 nm. The spectral repeatability of the ET-μFTIR is affected not only by the noises from the photodetectors and electronics but also by the tilting of the MEMS mirror. An interferogram from the sample can be expressed as [28]:

$$I_m = \mathrm{Ne}_m + c \cdot \sum_{k=1}^{N} B(\upsilon_k) \left\{ 1 + \frac{J_1(2\pi\upsilon_k\theta_m D)}{\pi\upsilon_k\theta_m D} \cos\left[2\pi\upsilon_k(x_m + 2(\theta_m d))\right] \right\} \tag{2}$$
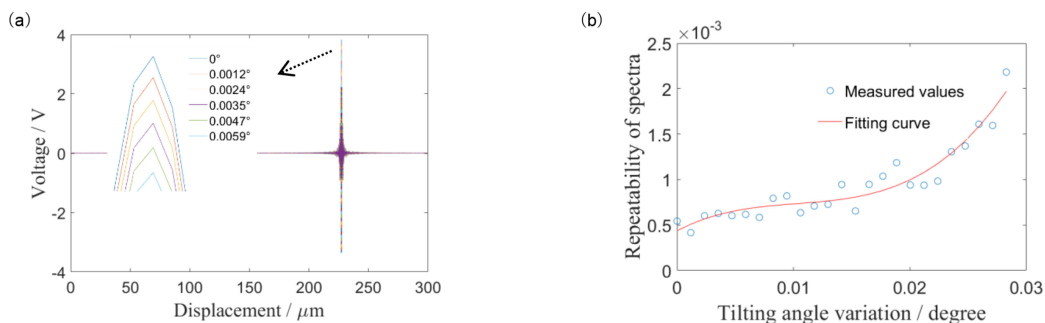
Fig. 5. (a) Interferograms at different variations of the MEMS tilting angle. (b) Spectral repeatability versus tilting angle variation.

where m stands for the mth point of the interferogram data, x_m is the corresponding optical path distance, θ_m stand for the tilting angles of the MEMS mirror. J1 is Bessel function of the first kind. D and d stand for the sample light spot diameter and the radius of MEMS mirror, respectively. Ne stands for the noise in signals, B is the spectral density of the light source, υ_k is the frequency of the kth wavelength. C is a constant value taken into account the light splitter ratio and the absorption losses along the optical path and set as 0.3 for simulation. After Fourier transform of the interferogram I_m, the absorption spectra, A_i^j can be obtained. By combining Eqs. (1) and (2), the spectral repeatability of the ET-μFTIR can be calculated. The optical path length corresponding to each MEMS mirror scan of 300 μm is equally divided into 12,500 data points, i.e., m in Eq. (2) is equal to 12,500. As the MEMS mirror is identical along both the x- and y- axis, the tilting angles θ_m is divided from $-0.01°$ to $0.01°$ in the calculation. During long-term use, θ_m will also gradually change by $\Delta\theta$ over time, which means the tilting angle will fluctuate from $-0.01° + \Delta\theta$ to $\Delta\theta$. 10 mV is set as the maximum value of Ne which is considered as random distribution. D and d are set as 1 mm and 0.6 mm, respectively. Fig. 5(a) presents the calculated interferograms with the tilting angle change of the MEMS mirror, $0.01° + \Delta\theta$, varying from 0 to 0.0059°. Note that the peak value decreases as the tilting angle increases. Fig. 5(b) plots the spectral repeatability versus variation of the tilting angle. The spectra were acquired over several days and the tilting angle was measured with a PSD. The spectral repeatability was calculated with Eq. (1). The spectral repeatability deteriorates to near 0.001 when the tilting angle reaches 0.02°, as shown in Fig. 5(b). For the soybean content detection application, the spectral repeatability must be controlled within 0.001 based on our extensive experimental study, so the MEMS tilting angle needs to be controlled within 0.02°.

2.3.2 Automatic MEMS Tilt Alignment: The initial position and tilt angle of the MEMS mirror plate may change over time, which will alter the interferograms generated by the DMI and thus deteriorate the spectral repeatability. In order to maintain the MEMS mirror at the same position and tilt angle of MEMS mirror for each use, a start-up automatic realignment algorithm is developed. The basic idea of the algorithm is to record the peaks of the interferogram at each stroke of the MEMS mirror and then tune the driving voltages of the MEMS mirror to match the peaks of the next interferogram. For simplicity, considering the MEMS mirror driven by four actuators (A1~A4) as shown in the schematic in Fig. 6(a), one pair (P1) of the actuators A1 and A2 shares one driving signal, while the other pair (P2) of the actuators A3 and A4 is connected to a different driving signal. The driving signals are triangular voltage waveforms ramping from 0.2 to 5 V in 100 ms. As shown in Fig. 6(b), two interferograms are generated from the DMI for each stroke of the MEMS mirror. The interferogram in red is from the sample while the interferogram in blue is from the reference laser. When the DMI is misaligned, the peak of the sample interferogram will decrease considerably, as the interferogram in green illustrates. Note that the ZPD point is also shifted. The two driving signals are provided by the digital analog converters (DACs) plus power amplifiers on PCB1.

The tilt alignment algorithm is illustrated in the block diagram as shown in Fig. 6(c). Upon a deterioration of the sample interferogram observed, the alignment algorithm is started. First, one of
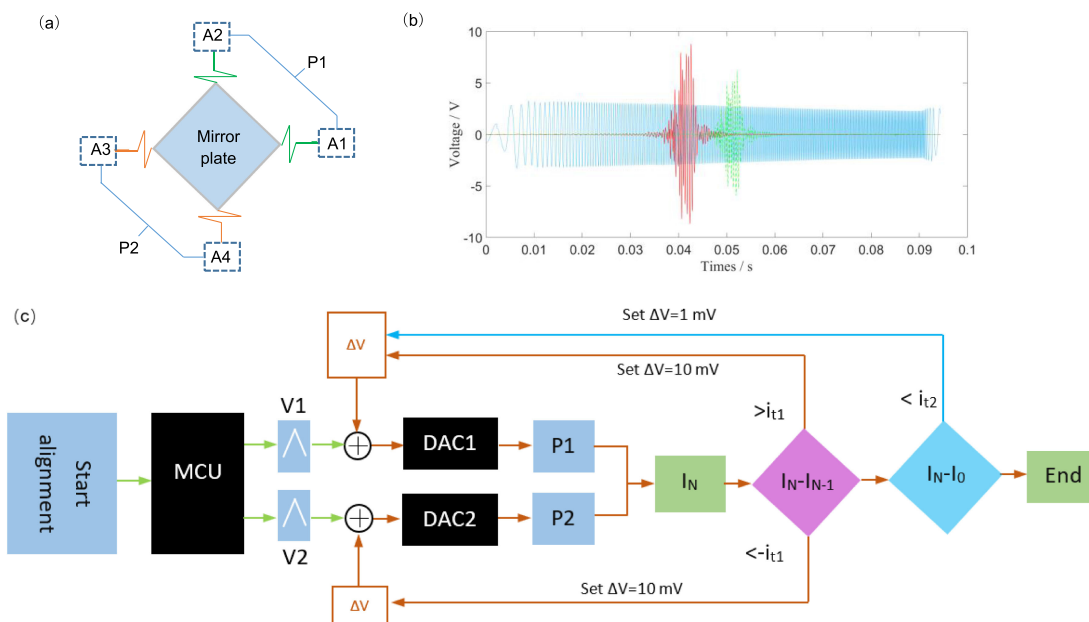
Fig. 6. (a) Simplified diagram of MEMS mirror driving method. (b) Interferograms of DMI with misalignment situation. (c) Block diagram of automatic MEMS tilt alignment algorithm. P1: pair of the actuators A1 and A2. P2: pair of the actuators A3 and A4. MCU: micro control unit. I_N:peak value of the sample interferogram. I_{N-1}:peak value of previous interferogram. i_{t1} is set as 200 mV, and i_{t2} is set as 10 mV. I_0: the recorded peak value of the sample interferogram.

the DACs adds a +10 mV bias to the driving voltage for P1. The corresponding peak value of the sample interferogram is detected and stored as I_N, where N is an integer. Then I_N is compared with the peak value, I_{N-1}, of the previous interferogram. If $I_N > I_{N-1}$, the drive voltage for P1 is increased by one more 10 mV. If $I_N < I_{N-1}$, then the drive voltage for P2 is increased by 10 mV. This process is repeated until the difference between I_N and I_{N-1} is near zero, i.e., less than a small value i_{t1}. After that I_N is compared to the recorded peak value, I_0. If $I_N < I_0$, the second loop is started with an increasing incremental voltage of 1 mV. After running this algorithm, the altered interferogram will be restored.

3. On-Site Soybeans Analyzer

A 3D model of the designed on-site soybean analyzer is shown in Fig. 7(a) with an inset showing a photo of the actual product. The diameter of the sample cup (SC) is 10 cm, and more than 200 mg soybeans (SN) can be loaded. Customers can use the touch screen (TS) to set the testing parameters and start the analysis procedure. Upon operation, the step motor (SM) rotates the sample cup around its center. A tungsten lamp is set at 44 mm from the bottom of the sample cup and points upward as sketched in Fig. 7(b). A fiber with a core diameter of 600 μm is employed to collect the back scattered light from the soybeans and guides it to the ET-μFTIR (MS). Note that the fiber has its own spectral response. Thus, the final spectra will be altered by the choice of the fiber. In other words, the prediction model may need to be re-calibrated if a different type of fiber is employed. The fiber tip points at 45° to the lamp light beam and is placed 31 mm away from the lamp. In order to establish accurate prediction models, more than 300 samples of soybeans across different locations were collected, and the weight of each sample was about 200 grams. Every sample was loaded into the sample cup three times, and each time one spectrum was acquired. The absorption spectrum of each sample is obtained by averaging the three spectra. Totally over 300 spectra were collected randomly from different locations.
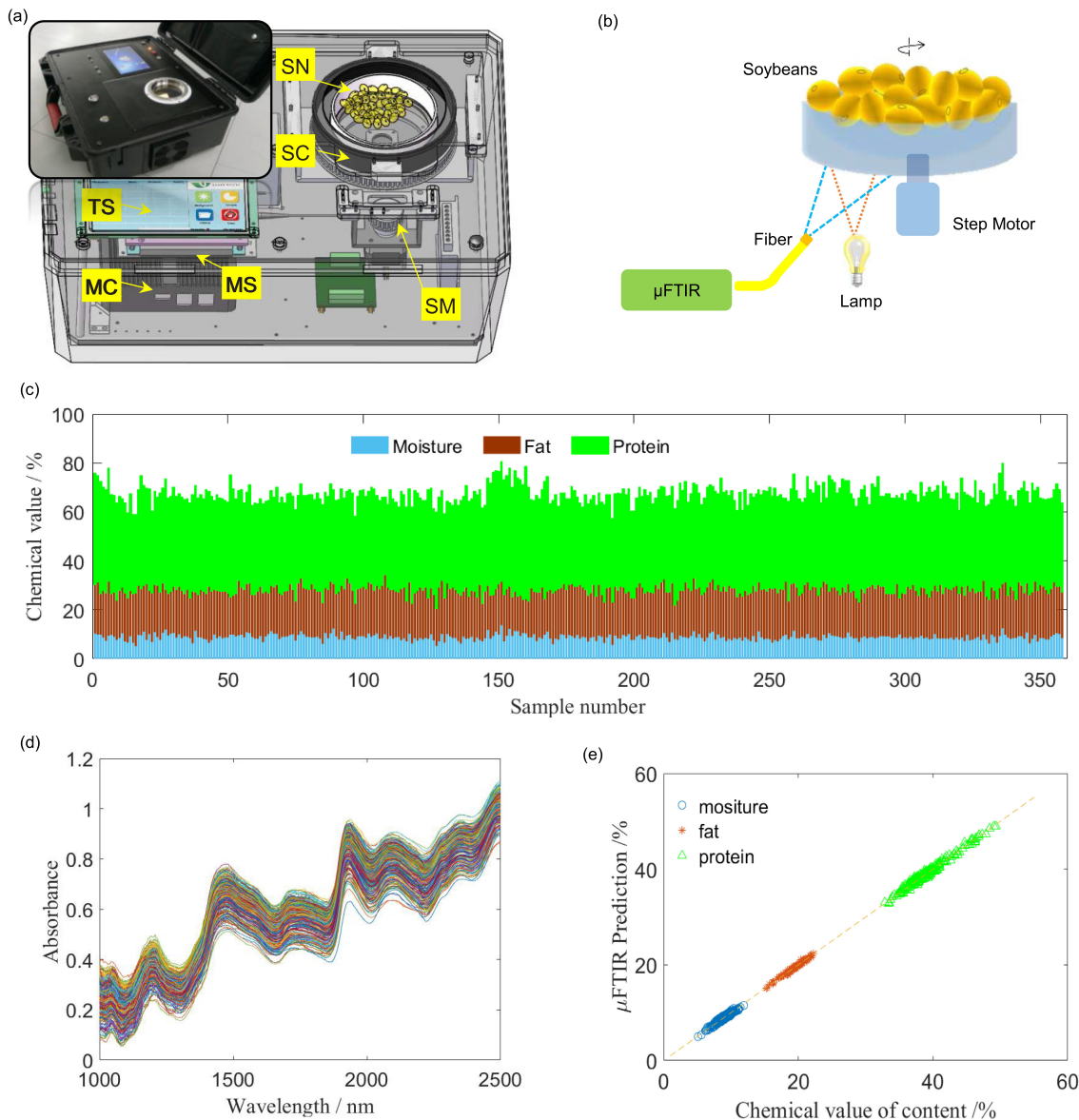
Fig. 7. (a) 3D design of the soybean analyzer. SN: soybeans. SC: sample cup. TS: touch screen. MC: minicomputer. MS: ET-μFTIR. SM: step motor. Inset: photo of the actual product. (b) Schematic diagram of the soybeans' composition detection. (c) Chemical values of main contents of 358 soybean samples. (d) Raw spectra of 358 soybean samples. (e) Prediction values versus true values of the soybean contents.

Fig. 7(c) plots the chemical values of the main contents (protein, fat and water) of 358 soybean samples obtained at a chemical analysis laboratory (Quality and technical supervision of Guangxi bureau, China). Fig. 7(d) presents the raw spectra of those 358 soybean samples obtained by the soybean analyzer. It can be seen that the spectra share the same absorbance peak wavelengths but with different peak values. After the spectra of the samples were obtained, the soybeans were shattered for stoichiometric analysis [1].

To establish a robust prediction model, 80% of the soybean spectra were selected as the calibration set and the remaining 20% were used as the validation set. A quantitative prediction model relating the soybean content values from the chemical determination to the preprocessed spectra

TABLE 1
Performance of the Prediction Model

Content	Water	Protein	Fat
Minimum prediction	5.1	32.8	15.1
Maximum prediction	11.9	49.3	22.3
SD	1.1	3.2	1.5
SEC	0.28	0.46	0.48
SEP	0.31	0.56	0.69
RPD	3.9	6.7	7.1
R^2	0.92	0.92	0.85

was established using a stoichiometry method based on all spectral data that were preprocessed. The preprocessing of the spectra consecutively applied multiplicative scatter correction (MSC), Savitzky-Golay (SG) smoothing, and the second-order derivative of SG. Partial least squares (PLS) regression was used to build the regression model, and the regression coefficients of the prediction model were calculated using a nonlinear iterative partial least squares (NIPAL) algorithm. Principal component analysis (PCA) was also adapted to reduce the number of latent variables. By calculating the root mean square (RMS) of prediction error between the chemical values and prediction values, the regression model was obtained by the best regression coefficients corresponding to the minimum RMS of the prediction error. More details about building the prediction model can be found in [22].

Fig. 7(e) plots both the chemical values (i.e., the true values shown in Fig. 7(d)) and the predicted values, showing that the soybean analyzer can accurately measure the contents of soybeans. Note that the contents are chemical relative values, instead of the absolute weight/mass. As the data show, the standard deviation of the predicted values from the true chemical values is no more than 3%.

Table 1 summarizes the performance of the prediction model. The second row is the numbers of the principle components used to establish the prediction model, and the second and third rows present the prediction range. The standard error of calibration (SEC) and standard error of validation (SEP) are close to each other, which means the distributions of the calibration and validation sets are reasonable. When SEC is smaller than 0.5, the regression model is considered to be accurate. The relative predictive determinant (RPD), which is the ratio of the standard deviation (SD) of the prediction value to SEC, also helps to judge the predictive ability of the model. The achieved RPD is more than 3, which means the model can precisely predict the contents of the soybeans, including moisture, fat and protein.

4. Conclusion

An soybean analyzer has been developed based on an ET-μFTIR. The enabling device of the ET-μFTIR is an electrothermal MEMS mirror. The MEMS mirror is packaged in a sealed chamber for stable piston scanning. Based on the test data of the ET-μFTIR, the spectral repeatability is calculated and the requirement of the minimum MEMS tilt misalignment is determined. An algorithm that can realign the MEMS mirror at each start-up has been successfully developed for the long-term use. An accurate prediction model has been established based on more than 300 samples and the prediction matches the true chemical values within 3%. This soybean analyzer can provide rapid on-site determination of moisture, fat and protein contents of soybeans and may be extended to many other application areas.

References

[1] USDA, *Grain Inspection Handbook*. New York, NY, USA: Soybeans. 2013.

[2] W. F. McClure, "204 years of near infrared technology: 1800-2003," *J. Near Infrared Spectrosc.*, vol. 11, no. 6, pp. 487–518, 2003.

[3] H. Büning-Pfaue, "Analysis of water in food by near infrared spectroscopy," *Food Chem.*, vol. 82, no. 1, pp. 107–115, 2003.

[4] I. V. Kovalenko, G. R. Rippke, and C. R. Hurburgh, "Determination of amino acid composition of soybeans (Glycine max) by near-infrared spectroscopy," *J. Agricultural Food Chem.*, vol. 54, no. 10, pp. 3485–3491, 2006.

[5] G. M. Yee, N. I. Maluf, P. A. Hing, M. Albin, and G. T. A. Kovacs, "Miniature spectrometers for biochemical analysis," *Sens. Actuators A, Phys.*, vol. 58, no. 1, pp. 61–66, 1997.

[6] J. Antila *et al.*, *MEMS- and MOEMS-Based Near-Infrared Spectrometers*. New York, NY, USA: Wiley, 2000.

[7] M. Kraft *et al.*, "Single-detector micro-electro-mechanical scanning grating spectrometer," *Anal. Bioanal. Chem.*, vol. 386, no. 5, pp. 1259–1266, 2006.

[8] T. Pügner, J. Knobbe, and H. Grüger, "Near-infrared grating spectrometer for mobile phone applications," *Appl. Spectrosc.*, vol. 70, no. 5, pp. 734–745, 2016.

[9] Y. Yamamoto *et al.*, "A rotational MEMS diffraction grating for realization of micro-sized spectroscope system,"in *Proc. 18th Int. Conf. Solid-State Sens., Actuators Microsyst.*, 2015, pp. 208–211.

[10] S. C. Truxal, N. T. Huang, and K. Kurabayashi, "A nano grating tunable MEMS optical filter for high-speed on-chip multispectral fluorescent detection," in *Proc. 31st Annu. Int. Conf. IEEE Eng. Med. Biol. Soc. Eng. Futur. Biomed.*, 2009, pp. 6693–6695.

[11] G. Lammel, S. Schweizer, S. Schiesser, and P. Renaud, "Tunable optical filter of porous silicon as key component for a MEMS spectrometer," *J. Microelectromech. Syst.*, vol. 11, no. 6, pp. 815–828, 2002.

[12] N. Neumann, "Tunable infrared detector with integrated micromachined fabry-perot filter," *J. Microlithogrpahy Microfabrication Microsyst.*, vol. 7, no. 2, 2008, Art. no. 021004.

[13] H. R. Seren, S. Holmstrom, N. P. Ayerden, J. Sharma, and H. Urey, "Lamellar-grating-based MEMS fourier transform spectrometer," *J. Microelectromech. Syst.*, vol. 21, no. 2, pp. 331–339, 2012.

[14] M. Pisani and M. Zucco, "Compact imaging spectrometer combining Fourier transform spectroscopy with a Fabry–Perot interferometer," *Opt. Exp.*, vol. 17, no. 10, pp. 8319–8331, 2016.

[15] K. Yu, D. Lee, U. Krishnamoorthy, N. Park, and O. Solgaard, "Micromachined fourier transform spectrometer on silicon optical bench platform," *Sens. Actuators A, Phys.*, vol. 130/131, pp. 523–530, 2006.

[16] H. Kim and D. G. Allen, "Using digital filters to obtain accurate trended urine glucose levels from toilet-deployable near-infrared spectrometers," *J. Anal. Bioanal. Tech.*, vol. 7, no. 5, pp. 5–8, 2016.

[17] M. Erfan, Y. M. Sabry, M. Sakr, B. Mortada, M. Medhat, and D. Khalil, "On-chip micro-electro-mechanical system fourier transform infrared (MEMS FT-IR) spectrometer-based gas sensing," *Appl. Spectrosc.*, vol. 70, no. 5, pp. 897–904, 2016.

[18] U. Wallrabe, C. Solf, J. Mohr, and J. G. Korvink, "Miniaturized fourier transform spectrometer for the near infrared wavelength regime incorporating an electromagnetic linear actuator," *Sens. Actuators A, Phys.*, vol. 123/124, pp. 459–467, 2005.

[19] L. Wu, A. Pais, S. R. Samuelson, S. Guo, and H. Xie, "A miniature fourier transform spectrometer by a large-vertical-displacement microelectromechanical mirror," in *Proc. Int. Conf. OSA Fourier Transform Spectrosc.*, 2009, Paper FWD4.

[20] N. P. Ayerden *et al.,* "High-speed broadband FTIR system using MEMS," *Appl. Opt.*, vol. 53, no. 31, pp. 7267–7272, 2014.

[21] T. Sandner, T. Grasshoff, E. Gaumont, H. Schenk, and A. Kenda, "Translatory MOEMS actuator and system integration for miniaturized fourier transform spectrometers," *J. Microlithography Microfabrication Microsyst.*, vol. 13, no. 1, 2014, Art. no. 011115.

[22] D. Wang *et al.*, "Fourier transform infrared spectrometer based on an electrothermal MEMS mirror," *Appl. Opt.*, vol. 57, no. 21, pp. 5956–5961, 2018.

[23] D. Wang, X. Han, H. Liu, Q. Chen, W. Wang, and H. Xie, "Portable fourier transform infrared spectrometer based on an electrothermal MEMS mirror," in *Proc. 19th Int. Conf. Solid-State Sens., Actuators Microsyst.*, 2017, pp. 265–268.

[24] W. Wang, Q. Chen, D. Wang, L. Zhou, and H. Xie, "A bi-directional large-stroke electrothermal MEMS mirror with minimal thermal and temporal drift," in *Proc. Int. Conf. IEEE Micro-Electro Mech. Syst.*, 2017, pp. 331–334.

[25] CODE V, Synopsys. [Online]. Available: https://optics.synopsys.com.

[26] K. Jia, S. Pal, and H. Xie, "An electrothermal tip–tilt–piston micromirror based on folded dual S-shaped bimorphs," *J. Microelectromech. Syst.*, vol. 18, no. 5, pp. 1004–1015, 2009.

[27] S. R. Samuelson and H. Xie, "A large piston displacement MEMS mirror with electrothermal ladder actuator arrays for ultra-low tilt applications," *J. Microelectromech. Syst.*, vol. 23, no. 1, pp. 39–49, 2014.

[28] L. B. Xiang, J. F. Yang, Z. Gao, and G. X. Liu, "On the tolerance of the mirror tilting in Fourier transform interferometer," *Acta Photonica Sinica*, vol. 26, no. 2, pp. 132–135, 1997.

[29] S. T. Todd and H. Xie, "An electrothermomechanical lumped element model of an electrothermal bimorph actuator," *J. Microelectromech. Syst.*, vol. 17, no. 1, pp. 213–225, Feb. 2008.